Structure and Oxygen Evolution Activity of β-NiOOH: Where are the Protons?

Qi Hu,[1,2] Yufeng Xue[2], Jianxi Kang[3], Ivan Scivetti,[4,7] Gilberto Teobaldi,[5,8] Annabella Selloni[6*], Lin Guo[3*], Li-Min Liu[2*]

1. Beijing Computational Science Research Center, Beijing 100193, China
2. School of Physics, Beihang University, Beijing 100191, China
3. School of Chemistry, Beihang University, Beijing 100191, China
4. Scientific Computing Department, STFC UKRI, Daresbury Laboratory, WA4 4FS Warrington, United Kingdom
5. School of Chemistry, University of Southampton, Highfield, SO17 1BJ Southampton, United Kingdom
6. Department of Chemistry, Princeton University, Princeton, NJ 08544, USA
7. Stephenson Institute for Renewable Energy, Department of Chemistry, University of Liverpool, L69 3BX Liverpool, United Kingdom
8. Scientific Computing Department, STFC UKRI, Rutherford Appleton Laboratory, Harwell Campus, OX11 0QX Didcot, United Kingdom

Email: liminliu@buaa.edu.cn; guolin@buaa.edu.cn; aselloni@princeton.edu

Abstract

Ni oxides and oxy-hydroxides (NiO_x) have been studied for long time as cathode materials for alkaline batteries and electrocatalysts for the oxygen evolution reaction (OER). Yet, understanding of the connection between their atomic and electronic structure and electrochemical performance or stability is still incomplete. In this work, we use first-principles density functional theory (DFT) calculations to revisit the structure, electronic properties and OER activity of β-NiOOH, the catalytically active phase of NiO_x. Following extensive DFT-based screening, we identify a hitherto overlooked structure characterized by a uniform distribution of H atoms on the NiO_2 layers. All the Ni^{3+} cations in this structure exhibit an identical $t_g^6 e_g^1$ electronic configuration with occupied $3d_{z2}$ orbital. Comparison of calculated bond-lengths with Extended X-ray Absorption Fine Structure (EXAFS) data unequivocally supports this structure relative to all other low energy configurations. Based on this structure, we uncover and detail defect-dominated OER mechanisms on the basal β-NiOOH (001) surface, with overpotentials as low as 0.39 V. The present results should provide a valuable contribution to ongoing efforts at understanding and developing enhanced transition-metal hydroxide catalysts for the OER.

Keywords: First Principles Calculations, Energy Conversion and Storage, NiOOH, Oxygen Evolution Reaction, Water splitting

INTRODUCTION

Since its first use as cathode material in alkaline batteries by Edison and Jungner in the 1900s[1,2], NiO_x has seen a considerable expansion in the range of its applications, becoming one of the most important materials in electrocatalysis.[3,4] In particular, the fact that, as catalyst for the oxygen evolution reaction (OER), NiO_x exhibits performance comparable to noble metal-based catalysts such as IrO_2 and RuO_2[5,6] has contributed substantially to the continued interest in this material.

As first discovered by Bode,[7] NiO_x can be electrochemically converted between its four main phases, namely β-$Ni(OH)_2$, α-$Ni(OH)_2$, β-NiOOH, and γ-NiOOH. The α-$Ni(OH)_2$ and γ-NiOOH are formed during overcharging and, due their layered structure, intercalate multiple species such as OH^-, H_2O, CO_3^{2-}, and others.[8–10] Their poorly crystallized structure makes their study rather difficult, due also to their electrolyte-dependent stability.[11] Structural characterization of the crystalline β-$Ni(OH)_2$ and β-NiOOH phases has proved relatively easier, albeit not free of challenges. Whereas the structure of β-$Ni(OH)_2$, with fully protonated O atoms, has been elucidated,[12] quantitative resolution of β-NiOOH, the catalytically active phase for the OER, has proved more challenging. In comparison to β-$Ni(OH)_2$, β-NiOOH contains only half of the H-atoms, opening the possibility of different distributions and distinct electronic and electrocatalytic properties.

Such a potential variability in the H-distribution has motivated numerous studies of the β-NiOOH structure.[13–17] EXAFS characterization has revealed that β-NiOOH typically contains two Ni-O bond-lengths: long bonds of about 2.03-2.10 Å, and short ones of 1.87-1.90 Å.[18–20] Although there are subtle deviations in the reported bond lengths, several EXAFS experiments have suggested that the ratio in the number of long to short Ni-O bonds is 2:4.[18–20] Different explanations of the 2:4 ratio have been proposed. Some groups have suggested that a Jahn-Teller distortion is the main driver behind the two detected ranges of bond-lengths.[19] Others attributed it to the incomplete oxidation of the Ni sites in the β-$Ni(OH)_2$→β-NiOOH electrochemical conversion.[21] Further High Resolution Transmission Electron Microscopy (HRTEM) investigations identified an ABAB stacking sequence of the oxygen layers in β-$Ni(OH)_2$, and ABCA stacking associated with doubling of the *c* axis periodicity for β-NiOOH.[22] Although these experimental results provide valuable information on the atomic structure of β-NiOOH, the detailed distribution of the H-atoms inside this layered material remains quantitatively unresolved, thus preventing a complete understanding of the connection

between H-distribution and electrocatalytic activity.

On the theoretical side, several studies have also been carried out to explain these experimental observations. Based on a genetic algorithm search combined with first principles calculations, Li *et al* proposed a structure where half of the Ni^{3+} cations undergo disproportionation to Ni^{2+} and Ni^{4+} ions[13]. In contrast, Tkalych *et al* reported calculations showing that low spin d^7 Ni^{3+} is always energetically favored and proposed a β-NiOOH structure with alternating rows of OH groups and O atoms.[14] These two structures have been used as a basis for additional theoretical studies,[17,23–28] but the uncertainty in the atomic structure of β-NiOOH still remains.[29] Given the dependence of the calculated OER activity on the atomic model,[23–27] it is critical to determine the structure and electronic properties of β-NiOOH in order to uncover the origin of the observed activity.

To contribute to this effort, in this work we present a new analysis and determination of the lowest energy structures of β-NiOOH based on first principles simulations. Our results indicate that structures with a simple uniform H distribution, resulting in the same local electronic configuration for all Ni^{3+} ions, are energetically favored. The calculated Ni-O bond-length ratio agrees with the EXAFS results, and enables pinning of its origin in the Jahn-Teller effect. Based on this structure, we identify defect-dominated OER mechanisms on the basal β-NiOOH (001) surface with overpotentials as low as 0.39 V.

METHODS

Our calculations were performed using first-principles Density Functional Theory (DFT), as implemented in the Vienna Ab Initio Simulation Package (VASP).[30,31] The general gradient approximation of Perdew-Burke-Ernzerhof (GGA-PBE) was used to describe the exchange-correlation (XC) functional.[32] Candidate structures for bulk β-NiOOH were explored using DFT+U with an effective U–J term of 5.5 eV, obtained from linear response calculations,[33] for Ni 3d states. The hybrid XC-functional HSE06 was used to confirm the lowest-energy configurations, following previously published benchmarking procedures.[34] In all calculations, van der Waals (vdW) interactions were accounted for at the D3 level.[35,36] We applied a plane wave cutoff of 500 eV to expand the electronic wave functions. We considered a bulk unit cell containing 8 NiOOH units and sampled reciprocal space using 6 × 6 × 4 Monkhorst-Pack (MP) grids[37] in the PBE+U and HSE06 calculations. The HF kernel for hybrid functionals is evaluated on subgrid of k points that is denoted the q-point mesh, which was down sampled to 3 × 3 × 2 to decrease the high computational cost. The structures were relaxed until the force on each atom was smaller than 0.01 eV/Å. The convergence criterion for the electronic

self-consistency was 10^{-6} eV. The symmetry was switched off during structural relaxation. The calculated bulk lattice parameters for each considered configuration are given in Table S1. Vibrational zero-point energies were not considered for the energy screening of competing structures as previously benchmarked not to affect the relative stability of different phases of Ni oxy-hydroxides.[11]

Bulk phonon dispersion curves for NiOOH were computed using a MP grid of 9 × 9 × 6 k-points. The 32-atom unit cell was fully optimized until the forces on all atoms were less than 10^{-3} eV/Å before performing the phonon calculations. Single site OER calculations were performed using four-layer (2 × 2) slabs (16 Ni atoms). We used two-layer slabs with (4 × 4) surface supercell (32 Ni atoms) to model the OER on the defective (001) surface. The formation energies of typical surface defects were examined as a function of number of layers in the slab. As shown in Table S8, two-layer slabs are sufficient to obtain surface defect formation energies converged to within less than 0.005 eV. Further details of the OER calculations can be found in the Supporting Information.

RESULTS and DISCUSSION

Structure and energetics

In $Ni(OH)_2$, all oxygen atoms are bonded to one H atom. Conversely, in β-NiOOH, only half of the oxygen atoms form OH groups, leaving the other half of the oxygen atoms two-fold coordinated. As a result, several arrangements of the H-atoms in β-NiOOH are possible. Here, we focus on four high-symmetry configurations, two of which have already been reported in previous studies.[13,14] These four configurations emerged from extensive screening of the possible arrangements during which we observed that a uniform dz^2 character for the Ni^{3+} sites was a recurrent feature that lowered the energy of the system.

In the first structure (β-NiOOH-**U**), the H atoms are uniformly distributed on top of every second O-atom along *x* to form a (2 × 2) pattern (Figure 1(a)). In the second structure, β-NiOOH-**S** in Figure 1(b), H atoms are present on one side only of the layers, leaving the other side devoid of any O-H bond. The third structure (β-NiOOH-**L**, Figure 1(c)) features alternate rows of O and OH along the y-axis[14]. The fourth structure (β-NiOOH-**M**, Figure 1(d)) is obtained by alternatively stacking fully hydroxylated $Ni(OH)_2$ and fully dehydroxylated NiO_2 layers[13]. It is important to note that, in spite of the different geometries, all these four structures have the same stoichiometry, which enables direct comparison of their calculated total energies. Also important for comparing total energies, all investigated structures with the exception of β-NiOOH-**S** do not have a dipole perpendicular to the NiO_x layers, which excludes artificial contribution to the total energy of the system due to periodic repetition of polar simulation cells (see also below).

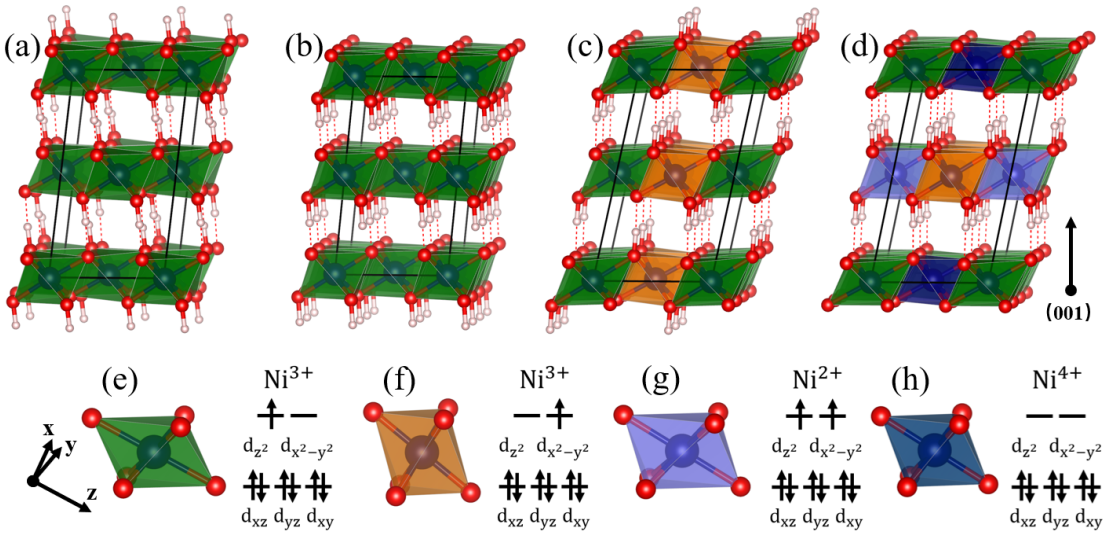

Figure 1. Atomic structure and electronic configuration of several β-NiOOH models. **(a)** β-NiOOH-**U** with a uniform distribution of H-atoms on both sides of the NiO_x layers, resulting in the same electronic configuration for each Ni ion. **(b)** β-NiOOH-**S** with H-atoms distributed over one side only of the layers. **(c)** β-NiOOH-**L** with H-atoms distributed over alternated rows of O-atoms on each side of the layers. **(d)** β-NiOOH-**M** with H-atoms distributed so as to form alternating $Ni(OH)_2$ and NiO_2 layers. **(e)-(h)** Octahedral crystal fields and electronic configurations of the inequivalent Ni ions in (a)-(d). The bulk unit cell used is indicated (black line).

We first analyze the relative energies and electronic configurations of the different structures in Figure 1. As shown in Table 1, β-NiOOH-**U** has the lowest energy, regardless of the XC-functional used. We notice that while a model with uniform H distribution was also considered in Ref.[15], its unit cell was not fully optimized, resulting in a structure 0.5 eV less stable than β-NiOOH-U with fully optimized unit cell. The projected density of states (PDOS) for each symmetry inequivalent Ni cation of β-NiOOH-**U** is shown in Figure S1 of the Supporting Information. All the Ni ions in the system exhibit the same electronic configuration, namely $t_{2g}^6e_g^1$ with the dz^2 orbital half occupied (Fig 1(e)). Because of a Jahn-Teller distortion and z-axis elongation induced by occupation of the dz^2 orbital, the apical Ni-O bonds, 2.05 Å, are ~ 0.17 Å longer than the other equatorial Ni-O bonds (1.88 Å).

As shown in Table 1, β-NiOOH-**S** is the highest energy structure for A|A and A|B stacking with PBE+U+D3 and A|A stacking with HSE06+D3. Interestingly, also this structure results in a uniform distribution of Ni^{3+} ions with half-occupied dz^2 orbitals (see Figure 1b, and 1e, and Figure S2), similar to β-NiOOH-**U**. In fact, each Ni ion of β-NiOOH-**S** resides in the same octahedral environment as in β-NiOOH-**U**. As already

pointed out, the distribution of H-atoms on one side only of the NiO_x layer generates an intrinsic polarization. In spite of the artificially stabilizing contributions of this polarization, the relative energy of β-NiOOH-**S** is the *highest* among all investigated systems. This result suggests that it is the coexistence of H-bonding acceptor and donor sites on each side of the NiO_x layers that is crucial for the stabilization of NiOOH.

Turning to the other structures in Figure 1, β-NiOOH-**L** is about 0.19 and 0.23 eV higher in energy than β-NiOOH-**U** with PBE+U+D3 and HSE06+D3, respectively (these values are referred to a unit cell containing 8 Ni ions, see Table 1). In this structure too, all the Ni ions are in a Ni^{3+} state. However, closer inspection of their electronic configurations reveals interesting differences. In β-NiOOH-**U**, all the Ni ions have the dz^2 orbital occupied. In contrast, for β-NiOOH-**L**, half of the Ni ions have occupied dz^2 orbitals, while in the other half the dx^2-y^2 orbital is occupied (Figure 1c, 1e, 1f, and Figure S3). Thus, while the overall electronic configurations for both β-NiOOH-**U** and β-NiOOH-**L** is $t_{2g}^6e_g^1$, the electronic configuration of the latter system is not uniform. As a consequence, β-NiOOH-**L** shows coexistence of differently distorted Ni-O bonds for the two different classes of Ni^{3+} ions: shrinking induced by occupation of the dx^2-y^2 orbital *and* elongation along the z-axis due to population of the dz^2 orbital.

The last structure in Figure 1, β-NiOOH-**M,** is energetically close to β-NiOOH-**L**, being about 0.19 and 0.39 eV per unit cell less stable than β-NiOOH-**U** at the PBE+U+D3 and HSE06+D3 levels, respectively. Although the structure suggests coexistence of $Ni(OH)_2$ and NiO_2 phases, the optimized electronic structure actually exhibits disproportionation, leading to a quarter of the Ni ions in a +2 state, a quarter in a +4 state, and the remaining half in a +3 state, which can be in turn separated in two different classes, depending on the occupation of the dz^2 or dx^2-y^2 orbital[13]. Due to the coexistence of electronically different Ni ions, the overall electron configuration for β-NiOOH-**M** is rather complex (Figure S4). The Ni^{2+} and Ni^{4+} exhibit $t_{2g}^6e_g^2$ (Figure 1g) and $t_{2g}^6e_g^0$ (Figure 1h) electronic configurations, respectively. Different from the result for Ni^{3+} ions, the crystal fields of the Ni^{2+}-O and Ni^{4+}-O octahedra are highly symmetric, resulting in 6 equivalent Ni-O bonds. As for the Ni^{3+} ions, they contain both dz^2 (Figure 1e) and dx^2-y^2 (Figure 1f) occupied orbitals, thus showing both shrinking and elongation of the Ni-O bonds along the z-axis, as previously discussed for β-NiOOH-**L**.

To explore the effect of different vdW corrections on the results of Table 1, we reoptimized the unit cells of the investigated β-NiOOH structures with D2 and without vdW corrections. The results, reported in Table S6 and S7, show that the relative

stabilities of the different phases are not affected by the use or neglect of vdW. We also checked the relative stabilities of β-NiOOH-U and the other phases using a larger (4 × 4) supercell. The results of this test indicate that the β-NiOOH-U structure remains the most stable, consistent with the results for the smaller (2 × 2) supercells. We further verified the thermodynamic and dynamic stability of β-NiOOH-U by calculating the bulk phonon spectrum. As shown in Figure S13, the phonon spectrum of β-NiOOH-U does not exhibit imaginary frequencies, confirming that this structure should be dynamically stable.

Table 1. Relative energies (in eV) per unit cell of different β-NiOOH structures with A|A or A|B stacking sequence, calculated using the PBE+U+D3 and HSE06+D3 functionals. Unit cells with 8 Ni atoms were used and ferromagnetic ordering was always considered (see below). The corresponding relative energies per Ni atom are given in parentheses (in meV). In the first column, A and B indicate in-plane distributions of the O-atoms in the NiO_2 layers. The separator "|" indicates the boundary between different layers.

Functional	Stacking	β-NiOOH-**U**	β-NiOOH-S	β-NiOOH-L	β-NiOOH-M
PBE+U+D3	A|A	**0.00 (0)**	0.52 (64)	0.19 (24)	0.19 (23)
	A|B	0.08 (11)	0.73 (91)	0.25 (30)	0.22 (27)
HSE06+D3	A|A	**0.00 (0)**	0.59 (74)	0.23 (28)	0.39 (48)
	A|B	0.13 (17)	0.75 (93)	0.31 (39)	0.94 (118)

To validate the DFT prediction that β-NiOOH-**U** is the lowest-energy structure, we compare the calculated Ni-O bond-lengths with the available EXAFS results[18,21]. The calculated Ni-O bond lengths of NiOOH, NiO_2 and $Ni(OH)_2$ at both PBE+U+D3 and HSE06+D3 levels are shown in Figure 2. We note that all the six Ni-O bonds in $Ni(OH)_2$ and NiO_2 have equal calculated lengths, in agreement with experiment.[11–14] As mentioned earlier, this is due to the high symmetry of Ni^{2+} and Ni^{4+} in their octahedral crystal fields. The bond length of 2.06 Å for $Ni(OH)_2$ calculated with HSE06+D3 is closer to the experimental value of 2.05 Å than the PBE+U+D3 one (2.08 Å). For NiO_2, PBE+U+D3 predicts a bond-length about 0.01 Å larger than the experimental one, while HSE06+D3 leads to bond-lengths about 0.02 Å shorter than experiment (1.86 Å). These deviations are very contained, indicating that both approaches are reliable.

Turning next to β-NiOOH, the EXAFS measurements indicate that the Ni-O bonds can be divided into two groups, long bonds (around 2.07 Å) and short bonds (around 1.88 Å)[18–20]. Our DFT+U results for β-NiOOH-**U** show the four equatorial bond-lengths to be around 1.88 Å, and the two apical bond lengths about 2.05 Å, in close agreement with the EXAFS data. These PBE+U+D3 trends are reproduced and corroborated by the HSE06+D3 results. The splitting into two longer and four shorter bonds is attributed

to the Jahn-Teller effect induced by single occupation of the dz^2 orbital. For β-NiOOH-**S**, our calculations show the same separation into short and long bonds as found for β-NiOOH-**U**. For the other two structures, β-NiOOH-**L** and β-NiOOH-**M**, the computed Ni-O bond-lengths exhibit a larger spread, between 1.84 Å and 2.12 Å. Although some calculated bond-lengths are close to the EXAFS-derived values of 1.88 Å and 2.07 Å, most of the DFT results lie in an intermediate region with an overall much poorer agreement with the experiment. Thus, we conclude that only structures with a uniform electronic configuration, i.e. either β-NiOOH-**U** or β-NiOOH-**S** lead to calculated bond-lengths in good qualitative and quantitative agreement with the EXAFS values. This finding combined with the markedly higher energy of β-NiOOH-**S** over β-NiOOH-**U** (Table 1), suggests the latter as the most plausible structure probed by the EXAFS measurements[18,21]. Moreover, as already pointed out, we calculated the bulk phonon spectrum of β-NiOOH-U, which indicates that this structure is stable (Figure S13).

The results presented so far were obtained assuming A|A stacking, where the O atoms across layers are right on top of each other, facilitating hydrogen bonding interactions (Figure 1; note that A|A corresponds to BAAB in the notation of Ref. [22]). Alternatively, we can consider A|B stacking of the layers (Figure S5), where the O atoms across layers are staggered as in $Ni(OH)_2$. Our calculations show the A|A stacking to be more stable than A|B regardless of the XC-functional and the structural model (Table 1).

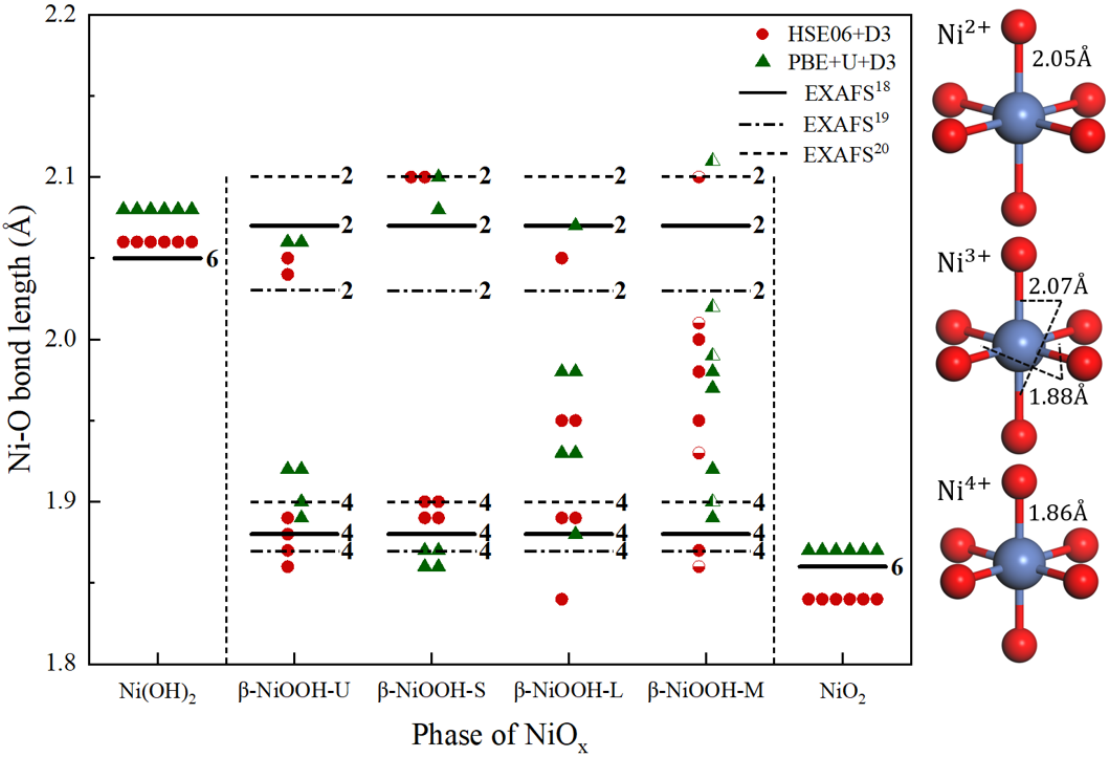

Figure 2. Comparison between EXAFS[18-20] and calculated (HSE06+D3, PBE+U+D3) Ni-O

bond-lengths for $Ni(OH)_2$, the different β-NiOOH structures in Figure 1, and NiO_2. The numeric labels 2, 4 and 6 indicate the experimentally determined number of Ni-O bonds per Ni ion having the reported bond-length. For $Ni(OH)_2$ and NiO_2, the Ni-O bond lengths are taken from Ref. 18. For NiOOH, the Ni-O bond lengths (2.07 Å and 1.88 Å) from Ref. 18 are shown as bold solid lines, Ni-O bond lengths from ref. 19 (2.03 Å and 1.87 Å) are shown as dashed lines, and Ni-O bond lengths from ref. 20 (2.10 Å and 1.90 Å) are shown as dash-dotted lines. The number of red circles and green triangles represents the computed average number of Ni-O bonds per Ni ion in the given structure. Full and half-filled symbols represent average values of one and half bond, respectively. Far right: experimentally derived atomic configuration for Ni^{2+} (six identical 2.05 Å NiO bonds), Ni^{3+} (four equatorial 1.88 Å Ni bonds of and two apical 2.07 Å ones) and Ni^{4+} (six identical 1.86 Å NiO bonds).

Given the relatively small energy differences among the different structures in Table 1, proton disorder and/or transition from the lowest-energy β-NiOOH-U structure to a different structure may be supposed to occur at room-temperature. To explore this possibility, we focused on calculating the inter-layer proton diffusion barriers. Interestingly, we found that proton diffusion in β-NiOOH-U occurs in pairs, that is, if one proton diffuses, another proton spontaneously diffuses as well. Thus, we have to explore the diffusion of two coupled protons. As shown in Figure S14, the diffusion of two coupled protons from the most stable configuration (β-NiOOH-U) exhibits an energy barrier of 0.46 eV. Instead, the energy barrier for the reverse process is only 0.03 eV. Thus, room temperature proton diffusion away from the β-NiOOH-U structure is hampered by a relatively large barrier (460 meV vs. 25 meV room-temperature thermal energy), suggesting that the β-NiOOH-U structure should be stable at room temperature. On the other hand, fluctuations of the proton distribution are very likely to occur at temperatures substantially higher than room-temperature. The other phases, e.g. β-NiOOH-L and β-NiOOH-M, may also occur under some conditions, in particular during oxidation and deprotonation of $Ni(OH)_2$.

Magnetic Ordering and Electronic Properties

The results in Table 1 were obtained assuming ferromagnetic (FM) ordering. We investigated the effect of magnetic ordering on the stability focusing on the energetically favored β-NiOOH-**U** (A|A-stacked) structure. The energies of different configurations are presented in Figure 3. The results show FM ordering to be indeed most stable and we thus restricted to FM configurations in most of our calculations. From Figure 3 it also appears, however, that the total energy difference between FM and antiferromagnetic (AFM) configurations is only 0.06 eV per unit cell (8 Ni ions), indicating that the contribution of magnetic interactions to the stability is extremely small.

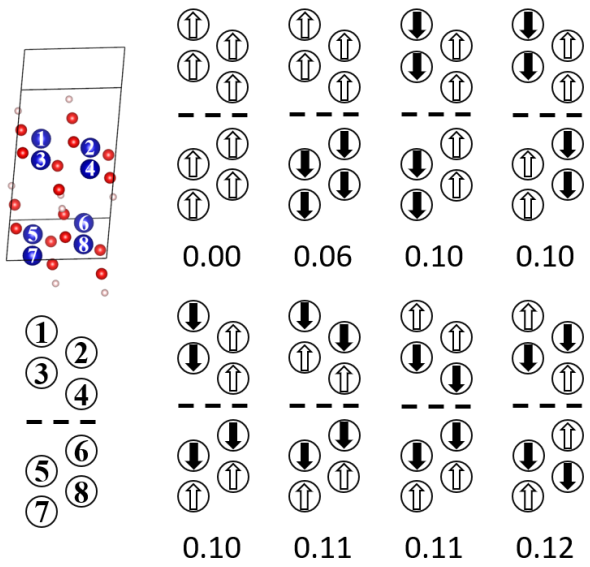

Figure 3. Calculated (PBE+U+D3) relative energies (eV) of different magnetic configurations for A|A-stacked β-NiOOH-**U**. The system contains two NiOOH layers, and each layer contains 4 Ni ions, for a total of 8 Ni ions per supercell. The dashed lines separate the upper and lower layer.

The electronic densities of states (DOS) for the different β-NiOOH structures (Figure 1) were calculated using the hybrid HSE06+D3 functional. As shown in Figure 4, β-NiOOH-**U** has the largest band-gap (2.12 eV), followed by β-NiOOH-**S** (1.91 eV), β-NiOOH-**L** (1.70 eV), and β-NiOOH-**M** (1.58 eV), indicating that the band gap decreases with increasing number of different electronic configurations of Ni ions in the structure. The computed band gap for the most stable β-NiOOH-**U** structure appears to be quite large in comparison to the experimental values of 1.7-1.8 eV[38] or even 1.5 eV[17] for the optical band gap of β-NiOOH, whereas β-NiOOH-**L** seems to be in better agreement with the experiments. As discussed in detail in Ref.[16] (with which our results for β-NiOOH-**L** agree closely), however, the 25% exact exchange fraction in the HSE06+D3 functional is larger than the optimal fraction for Ni oxy-hydroxides, leading to overestimated band gaps. In fact, a strong overestimate of the band gap is also found for $Ni(OH)_2$, for which the HSE06+D3 band gap is 4.75 eV (Figure S6) vs. an experimental value of ~ 3.-3.5 eV.[39] It seems thus safe to conclude that β-NiOOH-**U** gives the best agreement with experiment also for the electronic properties.

Figures 4e and 4f show the DOS of β-NiOOH-**U** containing an oxygen vacancy (Vo) and an OH vacancy (V_{OH}), respectively. Vo and V_{OH} introduce excess electrons (two and one, respectively) that occupy d_{x2-y2} orbitals and lead to the formation of Ni^{2+} ions. The corresponding defect states are found to lie deep in the band gap, close to the top of the valence band for the minority spins, and the resulting band gaps are 2.01 and

1.71 eV in the case of V_{OH} and V_O, respectively. Since defect states lie at the top of the valence band, we expect the band gap of β-NiOOH to decrease with increasing defect concentration thus enhancing the conductivity, as also predicted in a previous study.[40]

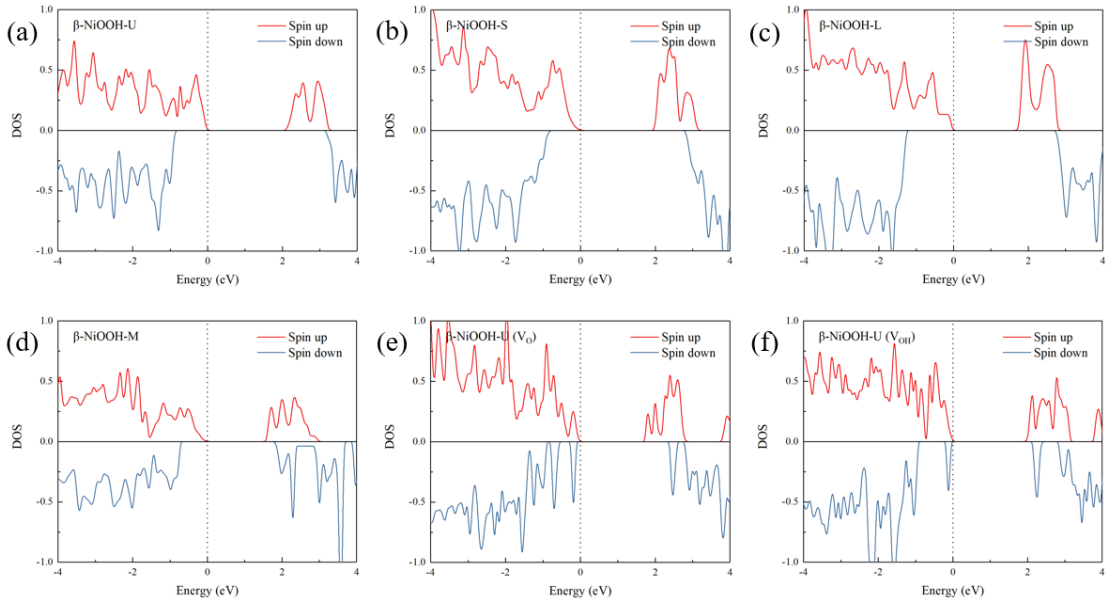

Figure 4. Calculated (HSE06) density of state (DOS) for **(a)** β-NiOOH-**U**, **(b)** β-NiOOH-**S**, **(c)** β-NiOOH-**L**, **(d)** β-NiOOH-**M**, **(e)** β-NiOOH-**U** with V_O, and **(f)** β-NiOOH-**U** with V_{OH}. The Fermi level is set at 0 eV.

Oxygen Evolution Reaction

Previous theoretical studies of the OER on β-NiOOH have often focused on step edges or high-index facets as active sites with lower overpotential[23,24,41,42]. Here we focus instead on the (001) basal surface, the most abundant for β-NiOOH (see computed surface energies in Table S4), for which relatively few studies have been reported.[16,43] As possible active sites for the reaction, we consider Vo and V_{OH}, which are expected to form under the typical applied potential of 1.5-1.6 V used for the OER. An applied potential of this magnitude is indeed smaller than the band gap of defect-free β-NiOOH, which can be estimated to be between 1.7-1.8 eV and 2.12 eV (see previous section). This should result in low conductivity and hole accumulation, which should in turn promote the creation of oxygen vacancies and related defects.

We investigated the OER activity of β-NiOOH based on the four steps mechanism proposed in Ref. [44]. The calculations were performed using PBE+U+D3. We only considered the *single-site* path for the OER, as test calculations for the *double-site* path[45] indicated a high relative energy of the key configuration shown in Figure S7. For the OER on β-NiOOH (001), there are only two groups of reactive sites, the OH and O

sites. In view of the high formation energy of *OOOH (*OOH at the O sites), only V_{OH} and V_O were considered as the active sites for the OER (Figure 5).

We start by comparing the activities of the energetically favorable β-NiOOH-**U**, β-NiOOH-**L** and β-NiOOH-**M** structures. The computed free energy diagrams for these structures are shown in Figure 5 and summarized in Table S2. For β-NiOOH-**U**, step 3 ($*O + H_2O \rightarrow *OOH + H^+ + e^-$) is rate-limiting at the V_O site, while step 2 ($*OH \rightarrow *O + H^+ + e^-$) is rate-limiting at the V_{OH} site, with calculated overpotentials of 0.74 and 0.53 V, respectively. The β-NiOOH-**L** structure exhibits a behavior similar to β-NiOOH-**U**, with calculated overpotentials of 0.60 V on V_O and 0.44 V on V_{OH}, in agreement with the results of Rajan et al.[16]. The rate-limiting step at the V_O and V_{OH} sites of β-NiOOH-**M** is also step 3, with calculated overpotentials of 0.44 and 0.55 V, respectively. To estimate how these results are affected by the solvent, we performed calculations of the OER at the V_O and V_{OH} sites on β-NiOOH-U with solvation correction.[46] The results (Figure S10) show that solvation changes the OER overpotential by no more than 0.03 eV and may thus be neglected. Similarly, we found that dipole corrections have a negligible effect on the calculated OER overpotential (Figure S11). To explore the role of kinetics, the pathways of O_2 desorption from the V_O and V_{OH} sites on β-NiOOH-U were also calculated using the Climbing Image Nudged Elastic Band (CI-NEB) method with 9 images.[47] The results show that the barrier between the adsorbed and desorbed states is equal to the O_2 desorption energy (Figure S12).

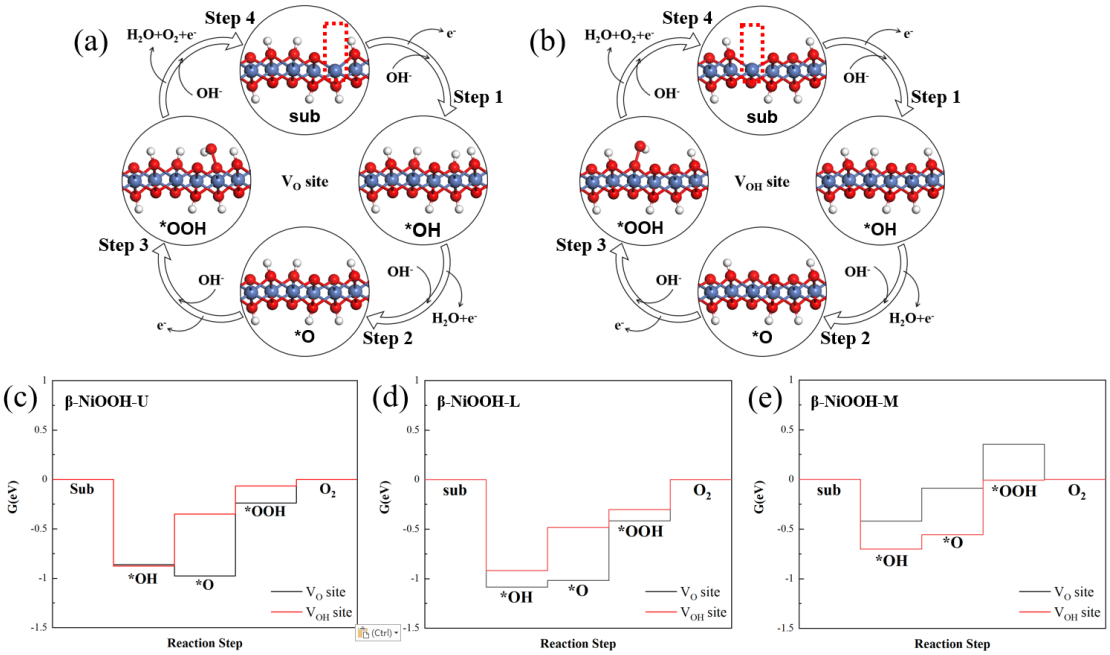

Figure 5 Investigated OER mechanism on potential reactive sites (in dashed red

rectangles) of β-NiOOH: **(a)** oxygen vacancy (V_O) and **(b)** hydroxyl vacancy (V_{OH}). **(c)-(e)** Calculated Gibbs free energy profiles of the four-electron OER process for β-NiOOH-**U**, β-NiOOH-**L** and β-NiOOH-**M**.

The fact that the overpotentials for β-NiOOH-**L** and β-NiOOH-**M** are smaller than those for the most stable β-NiOOH-**U** configuration indicates that it is essential to consider the most stable surface structure to obtain a reliable estimate of the OER overpotential and related properties. We will thus focus on further analysis of the OER mechanism on β-NiOOH-**U** in the following.

The calculated overpotential of 0.53 - 0.74 V for β-NiOOH-**U** (Figure 5c) is rather large compared with experiment and other theoretical estimates[23,24,43]. As a possible way of reducing it, we explored how extra defects, in addition to the reactive site, can affect the OER. Previous work on the performance of transition-metal (oxy)hydroxides for the OER has indeed shown that doping and defects can decrease the overpotential.[23,48–53] Moreover, the relatively low calculated formation energies for V_{OH} suggest that these defects can form quite easily (see Table S5). As pointed out above, defect formation should be further promoted by an applied potential**.**

We considered four typical defects that can form near the active site during the OER cycle in β-NiOOH-**U**: an additional V_O or V_{OH} defect, a deprotonated OH-group (**V_H**), and a protonated O-atom (**I_H**). We further considered 3 possible positions near the V_O or V_{OH} reactive site for each type of defect (see Figures S8 and S9) and altogether investigated 24 additional OER pathways on β-NiOOH-**U**. The corresponding Gibbs free energies are reported in Table S3. A volcano plot summarizing all calculated OER activities is shown in Figure 6a. Calculated values (dots) are interpolated by the line $\Delta G_{OOH}=\Delta G_{OH}+3.21$ eV with forced slope of 1 in Figure 6b, and the best fit relationship is $\Delta G_{OOH} = 0.98\Delta G_{OH} + 3.22$ eV. The R coefficient is 0.92 for both fitted functions, which are very close to the typical scaling relationship between the Gibbs free energy differences of *OH and *OOH found on metal and metal oxide surfaces.[54]

In order to understand why a deprotonated OH-group (V_H^1), and a protonated O-atom (I_H^3) could enhance the activity, we examined the relationship between the value of ΔG_{OH}-ΔG_{OOH} and the overpotential. As shown in Figure 6b, the difference between the absorption energy of the OH and OOH species is around 3.21 eV, thus the theoretical minimum overpotential is around 0.375 V when the difference in absorption energy for the O and OH species is around 1.605 eV. For the systems with V_O reactive sites, the difference between absorption energies of the O and OH species is around 1.2

eV, which leads to a higher overpotential of about 0.77 V. The overpotential concentrates mainly on the left side of the volcano plot, thus *O→ *OOH is the limiting step. In contrast, for the systems with V_{OH} reactive site, the adsorption difference comes to 1.65 eV, which is close to 1.605 eV. Thus, the overpotentials at the V_{OH} reactive sites are relatively small and mainly distributed in the middle of the volcano plot (Figure 6a and 6c). The minimum overpotentials are 0.41 V at the V_{OH} site with the V_O^3 defect, and 0.39 V at V_{OH} site with the V_H^1 and I_H^3 defects (Table S3), which is close to the center of the volcano. Thus, extra defects boost the OER activity by decreasing the overpotential. The physical origin of the effect is the capability of the extra defect to modulate the difference between the adsorption energy of O and OH.

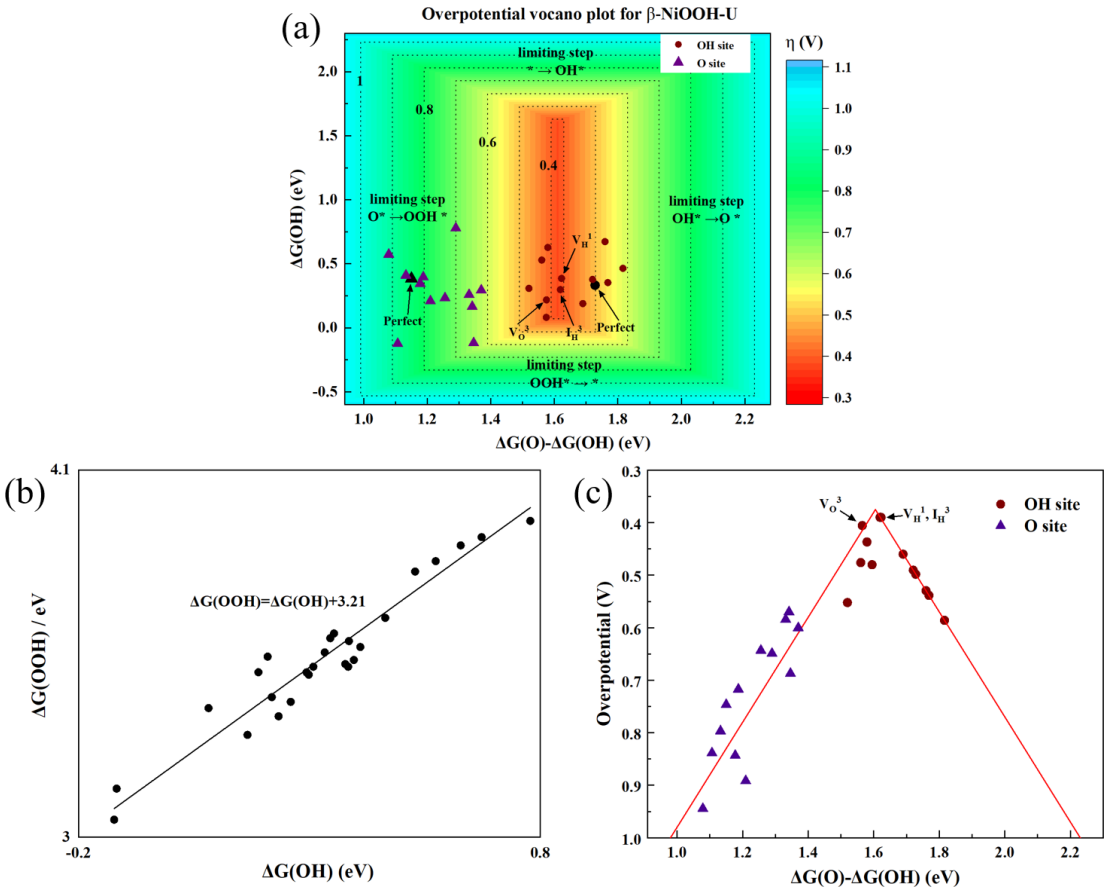

Figure 6. OER overpotential for β-NiOOH-**U. (a)** Volcano plot in the presence of additional V_O (purple triangles) and V_{OH} (red circles) reactive sites. The results for the pristine, defect-free ("Perfect") system on the volcano plot are marked by the black circle (single-V_O site) and triangle (single-V_{OH} site). **(b)** Scaling relationship between the adsorption Gibbs free energies of *OH and *OOH for all the considered β-NiOOH systems. Calculated values (dots) are interpolated by the line $\Delta G_{OOH}=\Delta G_{OH}+3.21$ eV. **(c)** Volcano plot in two-dimension, the center of the volcano is set to 1.605 eV, which corresponds to half of the average value of $\Delta G_{OH}-\Delta G_{OOH}$ (3.21 eV).

Conclusions

We have presented first-principles calculations of several low energy structures of β-NiOOH showing that the H distribution has a major influence on the atomic structure, electronic configuration, band gap and OER activity of this material. The most stable structure is characterized by a uniform H distribution and consistently exhibits a single electronic configuration for the Ni^{3+} ions with a half-occupied dz^2 orbital. As a result, the NiO_6 octahedra are Jahn-Teller distorted and characterized by two long apical and four short equatorial Ni-O bonds. Detailed comparison with EXAFS data unequivocally supports this structure relative to all other low energy configurations. Good agreement with experiments is also found for the electronic properties. Further investigation of the OER on the basal β-NiOOH (001) facet show that defects such as oxygen, hydroxyl and proton vacancies enhance the activity, leading to calculated overpotentials as low as 0.39 V. The new insights provided by our results should represent a useful contribution to the current efforts at developing layered hydroxide catalysts with enhanced OER activity.

ASSOCIATED CONTENT

Supporting Information

The Supporting Information is available free of charge on the ACS Publications website.

Results of various test calculations. Lattice parameters of the β-NiOOH structures. Calculated Gibbs free energies of the OER on V_O and V_{OH} reactive sites of different β-NiOOH structures. Calculated Gibbs free energies of the OER on V_O and V_{OH} reactive sites of defective β-NiOOH-U structures. Computed surface energies for the different β-NiOOH phases. Computed defect formation energies on the β-NiOOH (001) surface. Formation energies of different β-NiOOH structures using different functionals and van der Waals corrections. Computed surface defect formation energies as a function of the number of layers in the slab. Optimized coordinates of selected structures.

AUTHOR INFORMATION

Corresponding Authors

Annabella Selloni, Princeton University, Princeton, NJ 08544; Email: aselloni@princeton.edu

Lin Guo, School of Chemistry, Beihang University, Beijing 100191, China; Email: guolin@buaa.edu.cn

Li-Min Liu[2*] School of Physics, Beihang University, Beijing 100191, China; Email: liminliu@buaa.edu.cn;

ACKNOWLEDGMENTS

The work was supported by National Natural Science Foundation of China (51532001, 51861130360, 11974037), Beijing Natural Science Foundation (2194077), the National Postdoctoral Program for Innovative Talents (BX20180020). A.S. acknowledges the support of DoE-BES, Division of Chemical Sciences, Geosciences and Biosciences under Award DESC0007347. L.M.L. and G. T. acknowledge also support by the Royal Society Newton Advanced Fellowship scheme (grant No. NAF\R1\180242).

REFERENCES

(1) Edison, T. A. Reversible galvanic battery: U.S. Patent 678,722. 1901-7-16.
(2) Jungner, E. W. Electrode for reversible galvanic batteries: U.S. Patent 884,930. 1908-4-14.
(3) Reier, T.; Nong, H. N.; Teschner, D.; Schlögl, R.; Strasser, P. Electrocatalytic Oxygen Evolution Reaction in Acidic Environments. Reaction Mechanisms and Catalysts. 2016.
(4) Zhang, J.; Liu, J.; Xi, L.; Yu, Y.; Chen, N.; Sun, S.; Wang, W.; Lange, K. M.; Zhang, B. Single-atom Au/NiFe layered double hydroxide electrocatalyst: probing the origin of activity for oxygen evolution reaction. Journal of the American Chemical Society, 2018, 140(11): 3876-3879.
(5) Gao, M.; Sheng, W.; Zhuang, Z.; Fang, Q.; Gu, S.; Jiang, J.; Yan, Y. Efficient water oxidation using nanostructured α-nickel-hydroxide as an electrocatalyst. Journal of the American Chemical Society, 2014, 136(19): 7077-7084.
(6) Trotochaud, L.; Young, S. L.; Ranney, J. K.; Boettcher, S. W. Nickel–iron oxyhydroxide oxygen-evolution electrocatalysts: the role of intentional and incidental iron incorporation. Journal of the American Chemical Society, 2014, 136(18): 6744-6753.
(7) Bode, H.; Dehmelt, K.; Witte, J.; Zur kenntnis der nickelhydroxidelektrode—I. Über das nickel (II)-hydroxidhydrat. Electrochimica Acta, 1966, 11(8): 1079-1087.
(8) Van der Ven, A.; Morgan, D.; Meng, Y. S.; Ceder, G. Phase stability of nickel hydroxides and oxyhydroxides. Journal of The Electrochemical Society, 2005,

153(2): A210.
(9) Park, S.; Lee, Y.; Elcombe, M.; Vogt, T. Synthesis and Structure of the Bilayer Hydrate Na0. 3NiO2⊙1.3 D2O. Inorganic chemistry, 2006, 45(9): 3490-3492.
(10) Yang, X.; Takada, K.; Itose, M.; Ebina, Y.; Ma, R.; Fukuda, K.; Sasaki, T. Highly swollen layered nickel oxide with a trilayer hydrate structure. Chemistry of Materials, 2008, 20(2): 479-485.
(11) Wu, T. H.; Scivetti, I.; Chen, J. C.; Wang, J. A.; Teobaldi, G.; Hu, C. C.; Hardwick, L. J. Quantitative Resolution of Complex Stoichiometric Changes during Electrochemical Cycling by Density Functional Theory-Assisted Electrochemical Quartz Crystal Microbalance. ACS Applied Energy Materials, 2020, 3(4): 3347-3357.
(12) Oesten, R.; Wohlfahrt-Mehrens, M.; Ströbele, S.; Kasper, M.; Huggins, R. A. Structural aspects of undoped and doped nickel hydroxides. Ionics, 1996, 2(3): 293-301.
(13) Li, Y. F.; Selloni, A.; Mosaic texture and double c-axis periodicity of β-NiOOH: insights from first-principles and genetic algorithm calculations. The journal of physical chemistry letters, 2014, 5(22): 3981-3985.
(14) Tkalych, A. J.; Yu, K.; Carter, E. A.; Structural and electronic features of β-Ni (OH) 2 and β-NiOOH from first principles. The Journal of Physical Chemistry C, 2015, 119(43): 24315-24322.
(15) Martirez, J. M. P.; Carter, E. A.; Effects of the Aqueous Environment on the Stability and Chemistry of β-NiOOH Surfaces. Chemistry of Materials, 2018, 30(15): 5205-5219.
(16) Govind; Rajan, A.; Martirez, J. M. P.; Carter E A. Facet-independent oxygen evolution activity of pure β-NiOOH: different chemistries leading to similar overpotentials. Journal of the American Chemical Society, 2020, 142(7): 3600-3612.
(17) Goldsmith, Z. K.; Harshan, A. K.; Gerken, J. B.; Vörös, M.; Galli, G.; Stahl, S. S.; Hammes-Schiffer, S. Characterization of NiFe oxyhydroxide electrocatalysts by integrated electronic structure calculations and spectroelectrochemistry. Proceedings of the National Academy of Sciences, 2017, 114(12): 3050-3055.
(18) Pandya, K. I.; Hoffman, R. W.; McBreen, J.; O'Grady, W. E. In situ X-ray absorption spectroscopic studies of nickel oxide electrodes. Journal of The Electrochemical Society, 1990, 137(2): 383.
(19) Demourgues, A.; Gautier, L.; Chadwick, A. V.; Delmas, C. EXAFS study of the Jahn-Teller distortion in layered nickel oxyhydroxide. Nuclear Instruments and Methods in Physics Research Section B: Beam Interactions with Materials and Atoms, 1997, 133(1-4): 39-44.
(20) Bediako, D. K.; Lassalle-Kaiser, B.; Surendranath, Y.; Yano, J.; Yachandra, V. K.; Nocera, D. G. Structure–activity correlations in a nickel–borate oxygen evolution catalyst. Journal of the American Chemical Society, 2012, 134(15): 6801-6809.
(21) Capehart, T. W.; Corrigan, D. A.; Conell, R. S.; Pandya, K. I.; Hoffman, R. W.

In situ extended x-ray absorption fine structure spectroscopy of thin-film nickel hydroxide electrodes. Applied physics letters, 1991, 58(8): 865-867.
(22) Casas-Cabanas, M.; Canales-Vázquez, J.; Rodríguez-Carvajal, J.; Palacín, M. R. Deciphering the structural transformations during nickel oxyhydroxide electrode operation. Journal of the American Chemical Society, 2007, 129(18): 5840-5842.
(23) Friebel, D.; Louie, M. W.; Bajdich, M.; Sanwald, K. E.; Cai, Y.; Wise, A. M.; Cheng, M. J.; Sokaras, D.; Weng, T. C.; Alonso-Mori, R.; Davis, R. C.; Bargar, J. R.; Nørskov, J. K.; Nilsson, A.; Bell, A. T. Identification of highly active Fe sites in (Ni, Fe) OOH for electrocatalytic water splitting. Journal of the American Chemical Society, 2015, 137(3): 1305-1313.
(24) Li, L. F.; Li, Y. F.; Liu, Z. P.; Oxygen Evolution Activity on NiOOH Catalysts: Four-Coordinated Ni Cation as the Active Site and the Hydroperoxide Mechanism. ACS Catalysis, 2020, 10(4): 2581-2590.
(25) Dionigi, F.; Strasser, P. NiFe-based (oxy) hydroxide catalysts for oxygen evolution reaction in non-acidic electrolytes. Advanced Energy Materials, 2016, 6(23): 1600621.
(26) Tkalych, A. J.; Zhuang, H. L.; Carter, E. A. A density functional+ U assessment of oxygen evolution reaction mechanisms on β-NiOOH. ACS Catalysis, 2017, 7(8): 5329-5339.
(27) Fidelsky, V.; Toroker, M. C. Enhanced water oxidation catalysis of nickel oxyhydroxide through the addition of vacancies. The Journal of Physical Chemistry C, 2016, 120(44): 25405-25410.
(28) Conesa, J. C. Electronic structure of the (undoped and Fe-doped) NiOOH O2 evolution electrocatalyst. The Journal of Physical Chemistry C, 2016, 120(34): 18999-19010.
(29) Fidelsky, V.; Butera, V.; Zaffran, J.; Toroker, M. C. Three fundamental questions on one of our best water oxidation catalysts: a critical perspective. Theoretical Chemistry Accounts, 2016, 135(7): 1-5.
(30) Kresse, G.; Furthmüller, J. Efficient iterative schemes for ab initio total-energy calculations using a plane-wave basis set. Physical Review B, 1996, 54(16): 11169.
(31) Kresse, G.; Furthmüller, J. Efficient iterative schemes for ab initio total-energy calculations using a plane-wave basis set. Physical Review B, 1996, 54(16): 11169.
(32) Perdew, J. P.; Chevary, J. A.; Vosko, S. H.; Jackson, K. A.; Pederson, M. R.; Singh, D. J.; Fiolhais, C. Atoms, molecules, solids, and surfaces: Applications of the generalized gradient approximation for exchange and correlation. Physical Review B, 1992, 46(11): 6671.
(33) Cococcioni, M.; De Gironcoli, S. Linear response approach to the calculation of the effective interaction parameters in the LDA+ U method. Physical Review B, 2005, 71(3): 035105.
(34) Zaffran J, Caspary Toroker M. Benchmarking density functional theory based methods to model NiOOH material properties: Hubbard and van der Waals

corrections vs hybrid functionals. Journal of chemical theory and computation, 2016, 12(8): 3807-3812.
(35) Grimme, S.; Antony, J.; Ehrlich, S.; Krieg, H. A consistent and accurate ab initio parametrization of density functional dispersion correction (DFT-D) for the 94 elements H-Pu. The Journal of Chemical Physics, 2010, 132(15): 154104.
(36) Allouche, A. R. Gabedit—A graphical user interface for computational chemistry softwares. Journal of computational chemistry, 2011, 32(1): 174-182.
(37) Chadi, D. J. Special points for Brillouin-zone integrations. Physical Review B, 1977, 16(4): 1746.
(38) Carpenter, M. K.; Corrigan, D. A. Photoelectrochemistry of nickel hydroxide thin films. Journal of the Electrochemical Society, 1989, 136(4): 1022.
(39) Hermet, P.; Gourrier, L.; Bantignies, J.-L.; Ravot, D.; Michel, T.; Deabate, S.; Boulet, P.; Henn, F. Dielectric, Magnetic, and Phonon Properties of Nickel Hydroxide. Phys. Rev. B 2011, 84 (23), 235211.
(40) Dhaka, K.; Toroker, M. C. Revealing the Conducting Character of the β-NiOOH Catalyst through Defect Chemistry. The Journal of Physical Chemistry C, 2019, 123(31): 18895-18904.
(41) Martirez, J. M. P.; Carter, E. A. Secondary transition-metal dopants for enhanced electrochemical O2 formation and desorption on Fe-doped β-NiOOH. ACS Energy Letters, 2020, 5(3): 962-967.
(42) Martirez, J. M. P.; Carter, E. A. Unraveling oxygen evolution on iron-doped β-nickel oxyhydroxide: The key role of highly active molecular-like sites. Journal of the American Chemical Society, 2018, 141(1): 693-705.
(43) Tkalych, A. J.; Martirez, J. M. P.; Carter, E. A. Effect of transition-metal-ion dopants on the oxygen evolution reaction on NiOOH (001). Physical Chemistry Chemical Physics, 2018, 20(29): 19525-19531.
(44) Rossmeisl, J.; Logadottir, A.; Nørskov, J. K. Electrolysis of Water on (Oxidized) Metal Surfaces. Chem. Phys. 2005, 319 (1–3), 178–184.
(45) Huang, Z. F.; Song, J.; Du, Y.; Xi, S.; Dou, S.; Nsanzimana, J. M. V.; Wang, C.; Xu, Z. J.; Wang, X. Chemical and structural origin of lattice oxygen oxidation in Co–Zn oxyhydroxide oxygen evolution electrocatalysts. Nature Energy, 2019, 4(4): 329-338.
(46) Tripković, V.; Skúlason, E.; Siahrostami, S.; Nørskov, J. K.; Rossmeisl, J. The oxygen reduction reaction mechanism on Pt (1 1 1) from density functional theory calculations. Electrochimica Acta, 2010, 55(27): 7975-7981.
(47) Henkelman, G.; Uberuaga, B. P.; Jónsson, H. A climbing image nudged elastic band method for finding saddle points and minimum energy paths. The Journal of Chemical Physics, 2000, 113(22): 9901-9904.
(48) Xu, Q.; Jiang, H.; Duan, X.; Jiang, Z.; Hu, Y.; Boettcher, S. W.; Zhang, W.; Guo, S.; Li, C. Fluorination-enabled reconstruction of NiFe electrocatalysts for efficient water oxidation. Nano Letters, 2020, 21(1): 492-499.
(49) Jiang, J.; Sun, F.; Zhou, S.; Hu, W.; Zhang, H.; Dong, J.; Jiang, Z.; Zhao, J.; Li,

J.; Yan, W.; Wang, M. Atomic-level insight into super-efficient electrocatalytic oxygen evolution on iron and vanadium co-doped nickel (oxy) hydroxide. Nature communications, 2018, 9(1): 1-12.

(50) Liu, J.; Hu, Q.; Wang, Y.; Yang, Z.; Fan, X.; Liu, L. M.; Guo, L. Achieving delafossite analog by in situ electrochemical self-reconstruction as an oxygen-evolving catalyst. Proceedings of the National Academy of Sciences, 2020, 117(36): 21906-21913.

(51) Dionigi, F.; Zeng, Z.; Sinev, I.; Merzdorf, T.; Deshpande, S.; Lopez, M. B.; Kunze, S.; Zegkinoglou, I.; Sarodnik, H.; Fan, D.; Bergmann, A.; Drnec, J.; De Araujo, J. F.; Gliech, M.; Teschner, D.; Zhu, J.; Li, W.; Greeley, J.; Cuenya, B. R.; Strasser, P. In-situ structure and catalytic mechanism of NiFe and CoFe layered double hydroxides during oxygen evolution. Nature Communications, 2020, 11(1): 1-10.

(52) Wang, X.; Liu, X.; Tong, C. J.; Yuan, X.; Dong, W.; Lin, T.; Liu, L. M.; Huang, F. An electron injection promoted highly efficient electrocatalyst of FeNi 3@ GR@ Fe-NiOOH for oxygen evolution and rechargeable metal–air batteries. Journal of Materials Chemistry A, 2016, 4(20): 7762-7771.

(53) Bender, M. T.; Lam, Y. C.; Hammes-Schiffer, S.; Choi, K. S. Unraveling Two Pathways for Electrochemical Alcohol and Aldehyde Oxidation on NiOOH. Journal of the American Chemical Society, 2020, 142(51): 21538-21547.

(54) Man, I. C.; Su, H. Y.; Calle-Vallejo, F.; Hansen, H. A.; Martínez, J. I.; Inoglu, N. G.; Kitchin, J.; Jaramillo, T. F.; Nørskov, J. K.; Rossmeisl, J. Universality in oxygen evolution electrocatalysis on oxide surfaces. ChemCatChem, 2011, 3(7): 1159-1165.
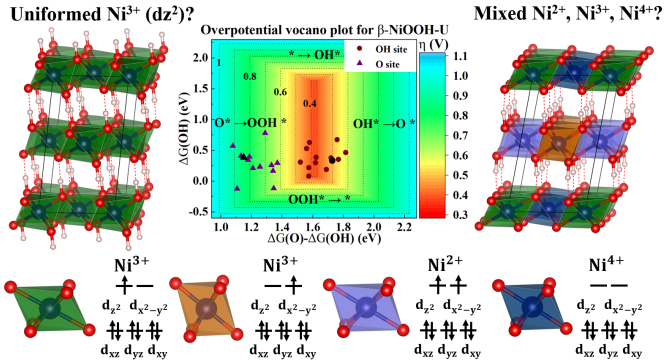
Table of Contents (TOC) graphic